PHYSICAL REVIEW B **96**, 081109(R) (2017)

# Large thermopower from dressed quasiparticles in the layered cobaltates and rhodates

Su-Di Chen,[1,2] Yu He,[1,2] Alfred Zong,[3,*] Yan Zhang,[2,4,†] Makoto Hashimoto,[5] Bin-Bin Zhang,[6,7] Shu-Hua Yao,[6,7] Yan-Bin Chen,[6,8] Jian Zhou,[6,7] Yan-Feng Chen,[6,9] Sung-Kwan Mo,[4] Zahid Hussain,[4] Donghui Lu,[5] and Zhi-Xun Shen[1,2,3,‡]

[1]*Department of Applied Physics, Stanford University, Stanford, California 94305, USA*
[2]*SIMES, SLAC National Accelerator Laboratory, Menlo Park, California 94025, USA*
[3]*Department of Physics, Stanford University, Stanford, California 94305, USA*
[4]*Advanced Light Source, Lawrence Berkeley National Laboratory, Berkeley, California 94720, USA*
[5]*Stanford Synchrotron Radiation Lightsource, SLAC National Accelerator Laboratory, Menlo Park, California 94025, USA*
[6]*National Laboratory of Solid State Microstructure, Nanjing University, Nanjing 210093, China*
[7]*Department of Materials Science and Engineering, Nanjing University, Nanjing 210093, China*
[8]*Department of Physics, Nanjing University, Nanjing 210093, China*
[9]*Collaborative Innovation Center of Advanced Microstructures, Nanjing University, Nanjing 210093, China*

(Received 25 July 2016; published 15 August 2017)

The origin of the large thermopower in $Na_xCoO_2$ is complicated by correlation phenomena. To disentangle the effects from multiple interactions, we use angle-resolved photoemission to study $K_xRhO_2$, an isostructural analogy of $Na_xCoO_2$ with large thermopower and weak electron correlation. Using the experimentally measured electronic structure, we demonstrate that the thermopower in $K_xRhO_2$ can be quantitatively explained within the quasiparticle framework after including an electron-phonon mass enhancement effect. Extending the analysis to the cobaltate, we find the doubling in thermopower is well accounted for by additional band renormalization from electron correlation. As such, the large thermopower emerges from the itinerant quasiparticles dressed by hierarchical electron-phonon and electron-electron interactions.

DOI: 10.1103/PhysRevB.96.081109

Thermoelectric materials are highly desirable for various energy applications including solid state cooling and heat-electricity conversion. Among these materials, oxides have attracted considerable research interest owing to their chemical and thermal stability [1]. A model system of thermoelectric oxides is the layered sodium cobaltate ($Na_xCoO_2$), a metal with a strikingly large thermopower [2,3]. Besides the thermopower, $Na_xCoO_2$ exhibits rich properties including Curie-Weiss-like susceptibility [4–6], spin-density-wave state [6–8], charge ordering [6,9], and hydration-induced superconductivity [10]. This richness, a reflection of participation of multiple interactions, also poses significant challenges for understanding the origin of the thermopower.

Two major scenarios have been proposed to explain the large thermopower in $Na_xCoO_2$. The first categorizes $Na_xCoO_2$ as a system where strong electron correlation leads to localization of carriers. In such systems, the flow of spin and orbital entropy accompanied by hopping-type conduction may cause a large thermopower [11–13]. This localized picture is supported by the Cure-Weiss-like susceptibility and field suppression of the thermopower [5,6], but rather hard to reconcile with the metallic resistivity of the sample [2,14]. An alternative scenario comes from the itinerant approach, where the thermopower is determined by the dispersion and scattering rate of quasiparticles. However, in $Na_xCoO_2$, this approach only qualitatively reproduces [15–17] the transport-measured thermopower due to complex effects from charge/spin ordering [6–9] and unusual electronic structure [18–23]. As a result, the origin of the large thermopower remains elusive.

Recently, a thermopower around half the size of $Na_xCoO_2$ was found in $K_xRhO_2$ ($x = 0.5, 0.62$), a $4d$ isostructural sibling of the cobaltate [24,25]. In this rhodate, resistivity measurements showed no sign of density waves [24,25]; optical study suggested weaker electron correlation and smaller carrier effective mass compared to those in $Na_xCoO_2$ [26]. Thus, the $K_xRhO_2$ system is ideal to help disentangle the correlation effects and unravel the origin of the large thermopower. To accomplish this task, obtaining accurate information about the electronic structure of $K_xRhO_2$ is clearly crucial.

In this work, we study the electronic structure of $K_xRhO_2$ ($x = 0.62$) using angle-resolved photoemission spectroscopy (ARPES). Three $t_{2g}$ bands are resolved near the Fermi level, with identical shapes but doubled bandwidth compared to those in $Na_xCoO_2$. Only one band crosses the Fermi level and forms a holelike Fermi pocket at the Brillouin zone (BZ) center. Reminiscent of the dispersion anomaly (kink) observed in the cobaltate, we find a prominent kink in the quasiparticle dispersion at around 70 meV binding energy, which we attribute to the coupling between electrons and phonons. Including this additional renormalization effect, we show that the transport-measured thermopower in $K_xRhO_2$ can be quantitatively reproduced using the band structure. Comparing $Na_xCoO_2$ to $K_xRhO_2$, we find the enhancement in thermopower is well accounted for by the additional band renormalization from electron correlation. Therefore, we conclude that the large thermopower in $Na_xCoO_2$ arises from the itinerant quasiparticles dressed by hierarchical electron-phonon and electron-electron interactions.

Single crystals of $K_{0.62}RhO_2$ were grown by the self-flux method [25]. ARPES measurements were performed at beam

*Present address: Department of Physics, Massachusetts Institute of Technology, Cambridge, Massachusetts 02139, USA.
†Present address: International Center for Quantum Materials, School of Physics, Peking University, and Collaborative Innovation Center of Quantum Matter, Beijing 100871, China.
‡zxshen@stanford.edu

 

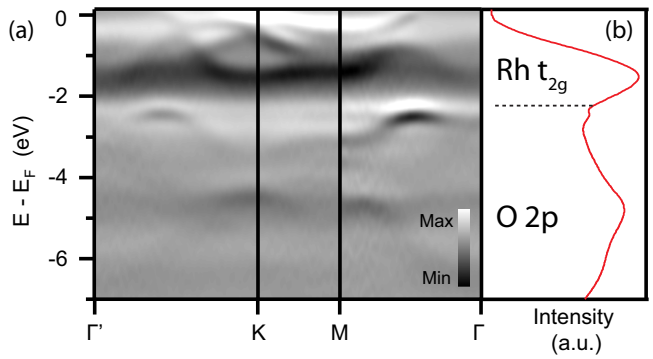


FIG. 1. Valence bands of $K_{0.62}RhO_2$. (a) Second derivatives of the photoemission intensity with respect to energy along the high-symmetry directions in the two-dimensional BZ. Γ′ denotes the Γ point in the next BZ. Dark areas correspond to band positions. (b) Integrated photoemission intensity over the momentum range in (a).

line 10.0.1 of the Advanced Light Source using a Scienta R4000 electron analyzer. The samples were cleaved *in situ* and measured at 20 K using 65 eV photons. The vacuum was better than $5 \times 10^{-11}$ torr throughout the measurements. The energy and angular resolutions were set to 30 meV and 0.3°, respectively.

Figure 1(a) shows the second derivatives of the photoemission intensity along the high-symmetry directions in the two-dimensional (2D) BZ [Fig. 2(a)]. The raw data are presented in the Supplemental Material [41], Fig. S1. A set of bands is resolved near the Fermi energy ($E_F$), well separated from the other bands at binding energies above 2 eV. The momentum-integrated photoemission intensity is also plotted in Fig. 1(b), where two broad peaks can be identified, centered at binding energies around 1.5 and 5 eV, respectively. According to the density functional theory (DFT) calculation [27], we attribute the features between 0 and 2 eV to the rhodium $4d$ $t_{2g}$ orbitals, and those between 2 and 7 eV to the oxygen $2p$ orbitals. Similar electronic structure has been reported in $Na_xCoO_2$, where the cobalt $3d$ $t_{2g}$ bands disperse within 1 eV from $E_F$, and the oxygen $2p$ bands reside between 2 and 6 eV [19,21,22].

Next, we study the detailed electronic structure of the $t_{2g}$ bands. At low binding energies, the quasiparticle dispersion is clearly resolved along both Γ-M and Γ-K directions in the ARPES spectra [Fig. 2(c), upper panels]. There is only one band crossing $E_F$, resulting in a single holelike pocket centered at the Γ point, as shown by the Fermi surface (FS) map in Fig. 2(a). Similar maps have been taken on another sample ($x = 0.59$) using photons from 40 to 70 eV (see Supplemental Material [41], Fig. S2), where the FS shows no dependence on photon energy, suggesting the 2D nature of the system at $x \approx 0.6$. The area enclosed by the FS is about 20% of the BZ area. This corresponds to a carrier density of 0.4 holes per Rh site according to the Luttinger theorem, which agrees with the stoichiometric K concentration $x = 0.62$. In contrast to $Na_xCoO_2$ [18,21,28], the hole pocket here has a weaker hexagonal character, which indicates the in-plane FS nesting condition of $K_xRhO_2$ is less ideal than that of $Na_xCoO_2$.

We further track down the dispersions of all three $t_{2g}$ bands [Figs. 2(b), 2(c) and 2(d)] and compare them with those in $Na_xCoO_2$ [22], as plotted in Fig. 2(e). The total occupied bandwidth of the $t_{2g}$ complex in the rhodate (1.6 eV) is twice as large as that of the cobaltate (0.8 eV) [22], reflecting a decrease of correlation among the $4d$ electrons compared to their $3d$ counterparts. Consequently, the reduced density of states near $E_F$ makes $K_xRhO_2$ less favorable for density wave instabilities than $Na_xCoO_2$.

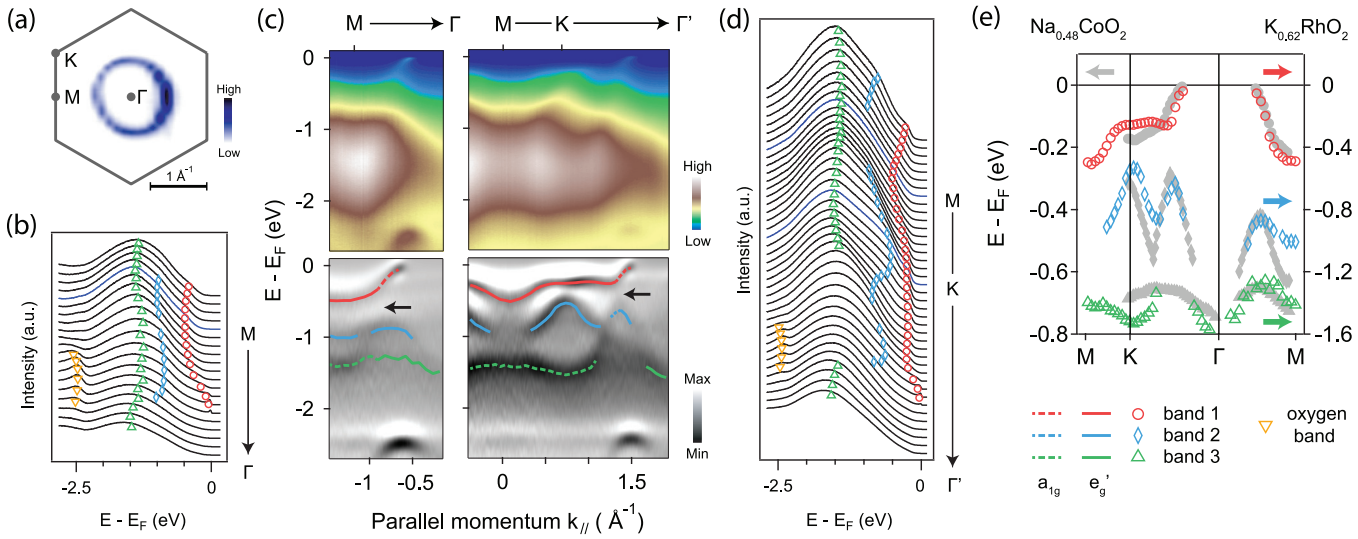


FIG. 2. Electronic structure of the $t_{2g}$ bands. (a) Photoemission intensity map integrated over the energy window ($E_F - 10$ meV, $E_F + 10$ meV). (c) Photoemission spectra (upper panels) and their second energy derivatives (lower panels) along Γ-M and Γ′-K-M directions. The dashed (solid) lines mark the band dispersions dominated by $a_{1g}$ ($e_g'$) orbital character, with their positions determined by the local minima of the image. The discontinuities appear where the local minima become less well defined. (b), (d) EDCs of the photoemission spectra from (c). The EDCs at M and K are plotted in blue. The markers denote the local minima from the second energy derivatives. (e) A comparison of the ARPES measured band structures of $K_xRhO_2$ and $Na_xCoO_2$ [22].

After rescaling along the energy axis, a good correspondence is found between the bands from the two systems [Fig. 2(e)]. With identical crystal symmetry and similar band structures, the orbital assignments for $Na_xCoO_2$ [15,29] should also apply to $K_xRhO_2$. In the $CoO_2$ and $RhO_2$ layers, the rhombohedral distortion of oxygen octahedra reorganizes the $t_{2g}$ triplet into one $a_{1g}$ and two $e'_g$ orbitals. The bands dominated by $a_{1g}$ and $e'_g$ orbital characters are illustrated by the dashed and solid curves in Fig. 2(c), respectively. Similarly to $Na_xCoO_2$ [22], strong orbital hybridization is present near the anticrossing points of the $a_{1g}$ and one of the $e'_g$ branches, as marked by the black arrows in Fig. 2(c). This hybridization separates the topmost hole band (band 1) from the deeper-lying two (band 2 and 3), making the orbital composition of band 1 momentum-dependent: $a_{1g}$ near the BZ center and $e'_g$ near the BZ boundary. We note that the occupied bandwidth of band 1 is around 0.5 eV, small compared to that of a simple metal [30], yet still much larger than the thermal energy at room temperature (∼26 meV).

In $Na_xCoO_2$, the DFT predicted $e'_g$ pockets near the K points [15] have been observed to sink below $E_F$ in ARPES experiments [18,19,21,22]. Several theoretical studies have been able to reproduce the ARPES band structure, including Gutzwiller-type approaches with large local Coulomb repulsion $U$ [20,31], dynamic mean field theory method with moderate $U$ [32], and DFT calculation considering disorder [33]. In $K_xRhO_2$, similar $e'_g$ pockets are also predicted [Fig. 4(b)] [27]. However, our data reveal that the topmost $e'_g$ dispersion is essentially flat near K at 0.25 eV below $E_F$. Interestingly, the total occupied bandwidth of the $t_{2g}$ complex is only renormalized by a factor of 1.15 from the DFT value [27], suggesting a weak electron correlation. Therefore, in $K_xRhO_2$, the sinking of the $e'_g$ pockets without strong electron correlation provides new opportunities to test the existing theories.

As the transport properties of a metal are usually governed by the quasiparticles near $E_F$, we now investigate the quasiparticle dispersion of $K_xRhO_2$. The photoemission spectra near the Fermi crossings along both Γ-K and Γ-M directions are plotted in Figs. 3(a) and 3(b), respectively. A kink in the dispersion is present, as indicated by the shaded bar around 70 meV in Fig. 3(c). The approximated real part of the electronic self-energy (ReΣ), obtained by subtracting a linear bare band from the dispersion, is also shown in Fig. 3(d). It is clear that ReΣ peaks around 70 meV along both Γ-K and Γ-M directions. A similar energy scale has been observed in $Na_xCoO_2$ and initially attributed to electron-boson coupling [18,21]. However, the anticrossing between the $a_{1g}$ and $e'_g$ bands happens around a similar energy, thereby making the origin of the kink less clear [22]. In $K_xRhO_2$, thanks to the increased bandwidth, the anticrossing happens at above ∼200 meV [black arrows in Fig. 2(c)], much higher than the kink energy. This apparent energy scale mismatch, together with the momentum-independent kink energy, rules out band anticrossing as the origin of the kink. On the other hand, inelastic neutron scattering on $K_xRhO_2$ has observed strong phonon density of states between 60 and 74 meV [34]; Raman measurements have also revealed phonon peaks around 62 meV [34]. We thus interpret the kink as a manifestation of electron-phonon coupling. Given the similarities in crystal and electronic structures, electron-phonon coupling should also contribute to the kink observed in $Na_xCoO_2$.

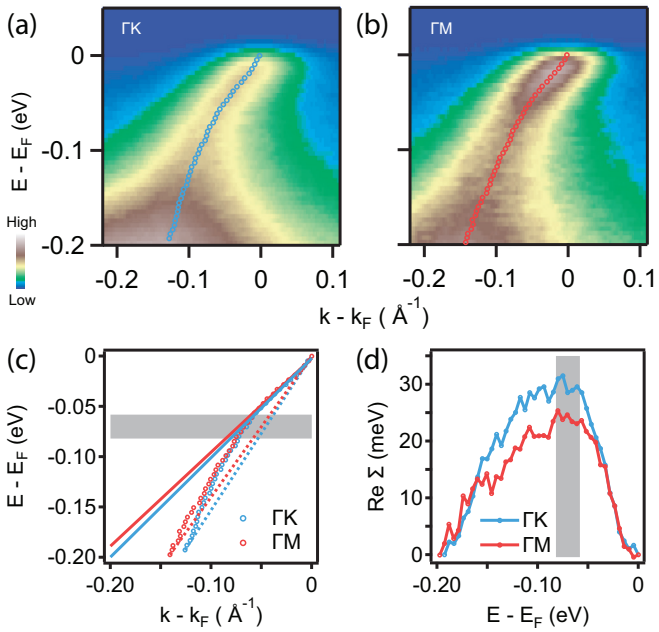


FIG. 3. Quasiparticle dispersion of $K_{0.62}RhO_2$. (a), (b) Photoemission spectra near $E_F$ along the Γ-K and Γ-M directions. The light dots mark the dispersion extracted by fitting each momentum distribution curve with a Lorentzian plus linear background. (c) Extracted dispersions from (a) and (b). The linear fits to the data between 0 and 50 meV are shown in solid lines. The shaded bar denotes the 70 meV kink position. (d) Real part of the electronic self-energy. The bare band is approximated by the dashed lines in (c).

To characterize this coupling in $K_xRhO_2$, we extract the Fermi velocity $v_F$ and the linear bare band velocity $v_L$ from experimental data. The ratio $R = v_L/v_F$ averaged between the Γ-K and Γ-M directions is around 1.53. To separate the effect from bare band curvature, we perform the same analysis on the DFT band structure [Fig. 4(b)] [27] and obtain $R_{\rm dft} \approx 1.1$. The mass enhancement from electron-phonon coupling $(1 + \lambda)$ is thus estimated to be $R/R_{\rm dft} \approx 1.4$.

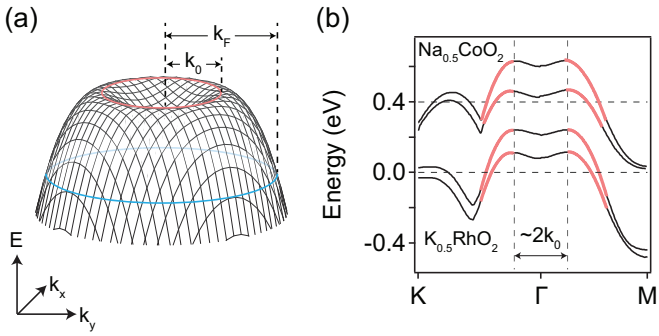


FIG. 4. The "pudding mold" dispersion of the band. (a) A schematic of the "pudding mold" band dispersion. The light blue and red curves denote the Fermi surface and the band top, respectively. (b) The band dispersions of $K_{0.5}RhO_2$ and $Na_{0.5}CoO_2$ (upshifted by 0.4 eV for clarity) from DFT calculations [15,27]. The fitting curves following Eq. (3) are shown in light red. The horizontal (vertical) dashed lines denote the position of $E_F$ (band top).

TABLE I. Estimation of the thermopower using ARPES data.

| | Averaged $v_F$ (eV Å) | Averaged $k_F$ (1/Å) | $k_0$ (1/Å) | Occupied $t_{2g}$ bandwidth (eV) | $S_{300\,\mathrm{K}}$ calculated ($\mu$ V/K) | $S_{300\,\mathrm{K}}$ measured ($\mu$ V/K) |
|---|---|---|---|---|---|---|
| $K_{0.62}RhO_2$ | 0.96 ± 0.02 | 0.55 ± 0.02 | 0.31 ± 0.05 | 1.6 | 46 ± 6 | 46 [25] |
| $Na_{0.57}CoO_2$ | 0.48 ± 0.1 [28] | 0.59 ± 0.1 [28] | 0.33 ± 0.05 [35] | 0.8 [22] | 85 ± 33 | 64–90 [2,5,36] |

With the electronic structure established, we now discuss possible origins of the large thermopower. In $Na_xCoO_2$, the localized picture is supported by the Cure-Weiss-like susceptibility and magnetic field suppression of the thermopower [5,6]. Interestingly, a Curie-Weiss-like divergence in susceptibility has also been found in $K_{0.62}RhO_2$ [25]. Since our data show that this system is only weakly correlated, we argue that the Curie-Weiss-like behavior alone cannot justify the existence of strong electron correlation and localized carriers. Theoretically, it has been shown that the Curie-Weiss-like behavior and field suppression of thermopower can be reconciled within an itinerant picture when the in-plane Stoner instability and $c$-axis exchange coupling are considered [31,37]. Indeed, our observation favors such itinerant scenarios.

Moreover, theories have shown that the thermopower only approaches the value from spin-and-orbital-entropy consideration when the thermal energy is comparable to or higher than the bandwidth [11,13]. Based on our data and previous ARPES results [22], the corresponding temperature scale would be much higher than $10^3$ K for both $Na_xCoO_2$ and $K_xRhO_2$, far exceeding the temperatures at which the thermopower is measured. Therefore, we conclude that the large thermopower observed around or below room temperature is not a direct consequence of the spin and orbital entropy. However, with the band structure being the other candidate, we remark that the spin and orbital degrees of freedom play important roles in shaping the electronic structure, and are ultimately related to the large thermopower.

We now estimate the thermopower within the itinerant quasiparticle framework. In a metal, at temperature $T$ much lower than the Fermi temperature, the thermopower is approximately given by the Mott formula [38],

$$S = \frac{\pi^2 k_B^2 T}{3e} \frac{d \ln \sigma(\epsilon)}{d\epsilon}\bigg|_{\epsilon=E_F}, \tag{1}$$

where $k_B$ is the Boltzmann constant, $e$ is the elementary charge, and $\sigma(\epsilon)$ is the electrical conductivity with the chemical potential at energy $\epsilon$. To simplify this formula, we assume the transport scattering rate has negligible energy dependence within $k_BT$ from $E_F$. Since the 2D electronic structure in $K_xRhO_2$ is only weakly anisotropic, $\sigma(\epsilon)$ in Eq. (1) can be replaced by $v(\epsilon)k(\epsilon)$, where $v$ is the band velocity and $k$ is the radius of the cylindrical constant-energy surface in the reciprocal space. These simplifications lead to

$$S = \frac{\pi^2 k_B^2 T}{3ev_F}\left(\frac{1}{k_F} + \frac{dv(\epsilon)}{d\epsilon}\right)\bigg|_{\epsilon=E_F}. \tag{2}$$

Here, $k_F$ is the size of the Fermi wave vector.

For a parabolic band, $dv(\epsilon)/d\epsilon|_{\epsilon=E_F} = 1/k_F$. However, previous ARPES measurements on the cobaltate have shown that the hole band actually has an unusual shape with a nearly flat top [35]. A schematic of this dispersion is plotted in Fig. 4(a). This "pudding mold" band shape is also present in the DFT calculations for both $Na_xCoO_2$ and $K_xRhO_2$ [Fig. 4(b)] [15,27], with its impact on thermopower discussed by Kuroki *et al.* [17].

To enable the extraction of $dv(\epsilon)/d\epsilon|_{\epsilon=E_F}$ from experimental data, we employ a minimal phenomenological model. We fit the dispersive part of the DFT bands above ($E_F - 0.1$ eV) to a parabolic function with a momentum offset,

$$E(k) = \alpha(|k| - k_0)^2 + \beta, \tag{3}$$

where $\alpha$, $\beta$, and $k_0$ are fitting parameters. Since the kink is absent in the DFT bands, the fit works well for both $Na_xCoO_2$ and $K_xRhO_2$, as shown by the light red curves in Fig. 4(b). In all the fits, $k_0 \simeq (0.30 \pm 0.05)\pi/a$, where $a$ is the in-plane lattice constant for the $CoO_2$ or $RhO_2$ layers. In fact, $k_0$ is simply the radius of the less dispersive part of the band, namely, the momentum difference between $\Gamma$ and the real band top [Fig. 4(a)], which is not sensitive to the strength of electron correlation. The $k_0$ value we obtained here is also consistent with the ARPES data of $Na_{0.85}CoO_2$ [35]. Using Eq. (3), we get $dv(\epsilon)/d\epsilon|_{\epsilon=E_F} = 1/(k_F - k_0)$. This equation remains valid with the inclusion of renormalization effects, since the renormalization factors in $E(k)$ always cancel out in $dv/d\epsilon$. Therefore,

$$S = \frac{\pi^2 k_B^2 T}{3ev_F}\left(\frac{1}{k_F} + \frac{1}{k_F - k_0}\right). \tag{4}$$

With experimentally measured $v_F$ and $k_F$, Eq. (4) gives a room temperature thermopower $S_{300\,\mathrm{K}} = 46 \pm 6\ \mu$V/K for $K_{0.62}RhO_2$, which is in quantitative agreement with the transport-measured value (Table I). We thus establish $K_xRhO_2$ as a clean case where the thermopower is purely from the phonon-renormalized band structure.

We now consider $Na_xCoO_2$ at a similar doping level. Utilizing the ARPES data from previous results [22,28], we find $S_{300\,\mathrm{K}}$ of $Na_{0.57}CoO_2$ to be around 85 $\mu$V/K (Table I), consistent with the transport measurements [2,5,36]. Given the similar kink structure in the low-energy quasiparticle dispersions, the doubling of $S_{300\,\mathrm{K}}$ from $K_xRhO_2$ to $Na_xCoO_2$ is accounted for by the overall bandwidth renormalization due to increased electron correlation. Thus, the large thermopower in $Na_xCoO_2$ is a consequence of hierarchical interactions of electron-electron and electron-phonon on top of each other.

We briefly remark on the doping dependence of the thermopower. Assuming a rigid band picture, increasing doping simply raises the chemical potential and reduces both $k_F$ and $v_F$. According to Eq. (4), this would further enhance the thermopower, which agrees with previous transport observations [3]. However, the actual effect of doping in $Na_xCoO_2$ is more complex. For $x > 0.7$, the electronic structure becomes

three-dimensional and anisotropic [23,35]; a Lifshitz transition also happens within this doping range [35]. Moreover, for $x = 0.5$ and $x > 0.7$, the band structure can be altered by the density-wave states [6–8]. Because none of these effects invalidate the quasiparticle framework, in this study, we choose to focus on a representative doping level and elucidate the essential physics. To generalize our minimal model to all dopings, future work needs to be done to include the evolution of quasiparticle dispersions and scattering rates beyond the rigid band picture.

Finally, we emphasize the importance of electron-boson coupling in enhancing the thermopower. In $Na_xCoO_2$ and $K_xRhO_2$, while the "pudding mold" band shape [17] and small bandwidth contribute to the large thermopower, electron-phonon coupling gives additional enhancement by renormalizing the band structure near $E_F$. In the thermoelectric misfit cobaltates with similar $CoO_2$ layers, prominent dispersion anomalies have also been reported [39,40]. Although the involved bosonic modes could be different, the role of electron-boson coupling should not be overlooked when evaluating the thermopower in the cobaltate and rhodate families.

We thank H. Pfau, K. Wu, J. He, and E. Yue Ma for helpful discussions. ARPES experiments were performed at the Advanced Light Source, which is a DOE Office of Science User Facility under Contract No. DE-AC02-05CH11231. The work at Stanford was supported by the DOE, Office of Science, Basic Energy Sciences, Division of Materials Science and Engineering, under Contract No. DE-AC02-76SF00515. The work at Nanjing University was supported by the National Natural Science Foundation of China (No. 11374149, No. 11574131 and No. 91622122).

[1] J. He, Y. Liu, and R. Funahashi, J. Mater. Res. **26**, 1762 (2011).
[2] I. Terasaki, Y. Sasago, and K. Uchinokura, Phys. Rev. B **56**, R12685 (1997).
[3] M. Lee, L. Viciu, L. Li, Y. Wang, M. L. Foo, S. Watauchi, R. A. Pascal, R. J. Cava, and N. P. Ong, Nat. Mater. **5**, 537 (2006).
[4] R. Ray, A. Ghoshray, K. Ghoshray, and S. Nakamura, Phys. Rev. B **59**, 9454 (1999).
[5] Y. Wang, N. S. Rogado, R. J. Cava, and N. P. Ong, Nature (London) **423**, 425 (2003).
[6] M. L. Foo, Y. Wang, S. Watauchi, H. W. Zandbergen, T. He, R. J. Cava, and N. P. Ong, Phys. Rev. Lett. **92**, 247001 (2004).
[7] L. M. Helme, A. T. Boothroyd, R. Coldea, D. Prabhakaran, D. A. Tennant, A. Hiess, and J. Kulda, Phys. Rev. Lett. **94**, 157206 (2005).
[8] S. P. Bayrakci, I. Mirebeau, P. Bourges, Y. Sidis, M. Enderle, J. Mesot, D. P. Chen, C. T. Lin, and B. Keimer, Phys. Rev. Lett. **94**, 157205 (2005).
[9] D. Qian, L. Wray, D. Hsieh, D. Wu, J. L. Luo, N. L. Wang, A. Kuprin, A. Fedorov, R. J. Cava, L. Viciu, and M. Z. Hasan, Phys. Rev. Lett. **96**, 046407 (2006).
[10] K. Takada, H. Sakurai, E. Takayama-Muromachi, F. Izumi, R. A. Dilanian, and T. Sasaki, Nature (London) **422**, 53 (2003).
[11] P. M. Chaikin and G. Beni, Phys. Rev. B **13**, 647 (1976).
[12] W. Koshibae, K. Tsutsui, and S. Maekawa, Phys. Rev. B **62**, 6869 (2000).
[13] W. Koshibae and S. Maekawa, Phys. Rev. Lett. **87**, 236603 (2001).
[14] S. Y. Li, L. Taillefer, D. G. Hawthorn, M. A. Tanatar, J. Paglione, M. Sutherland, R. W. Hill, C. H. Wang, and X. H. Chen, Phys. Rev. Lett. **93**, 056401 (2004).
[15] D. J. Singh, Phys. Rev. B **61**, 13397 (2000).
[16] T. Takeuchi, T. Kondo, T. Takami, H. Takahashi, H. Ikuta, U. Mizutani, K. Soda, R. Funahashi, M. Shikano, M. Mikami, S. Tsuda, T. Yokoya, S. Shin, and T. Muro, Phys. Rev. B **69**, 125410 (2004).
[17] K. Kuroki and R. Arita, J. Phys. Soc. Jpn. **76**, 083707 (2007).
[18] M. Z. Hasan, Y.-D. Chuang, D. Qian, Y. W. Li, Y. Kong, A. P. Kuprin, A. V. Fedorov, R. Kimmerling, E. Rotenberg, K. Rossnagel, Z. Hussain, H. Koh, N. S. Rogado, M. L. Foo, and R. J. Cava, Phys. Rev. Lett. **92**, 246402 (2004).
[19] H. B. Yang, S. C. Wang, A. K. P. Sekharan, H. Matsui, S. Souma, T. Sato, T. Takahashi, T. Takeuchi, J. C. Campuzano, R. Jin, B. C. Sales, D. Mandrus, Z. Wang, and H. Ding, Phys. Rev. Lett. **92**, 246403 (2004).
[20] S. Zhou, M. Gao, H. Ding, P. A. Lee, and Z. Wang, Phys. Rev. Lett. **94**, 206401 (2005).
[21] H.-B. Yang, Z.-H. Pan, A. K. P. Sekharan, T. Sato, S. Souma, T. Takahashi, R. Jin, B. C. Sales, D. Mandrus, A. V. Fedorov, Z. Wang, and H. Ding, Phys. Rev. Lett. **95**, 146401 (2005).
[22] D. Qian, L. Wray, D. Hsieh, L. Viciu, R. J. Cava, J. L. Luo, D. Wu, N. L. Wang, and M. Z. Hasan, Phys. Rev. Lett. **97**, 186405 (2006).
[23] J. Geck, S. V. Borisenko, H. Berger, H. Eschrig, J. Fink, M. Knupfer, K. Koepernik, A. Koitzsch, A. A. Kordyuk, V. B. Zabolotnyy, and B. Büchner, Phys. Rev. Lett. **99**, 046403 (2007).
[24] S. Shibasaki, T. Nakano, I. Terasaki, K. Yubuta, and T. Kajitani, J. Phys.: Condens. Matter **22**, 115603 (2010).
[25] S. H. Yao, B. B. Zhang, J. Zhou, Y. B. Chen, S. T. Zhang, Z. B. Gu, S. T. Dong, and Y. F. Chen, AIP Adv. **2**, 042140 (2012).
[26] R. Okazaki, Y. Nishina, Y. Yasui, S. Shibasaki, and I. Terasaki, Phys. Rev. B **84**, 075110 (2011).
[27] Y. Saeed, N. Singh, and U. Schwingenschlögl, Adv. Funct. Mater. **22**, 2792 (2012).
[28] D. Qian, D. Hsieh, L. Wray, Y.-D. Chuang, A. Fedorov, D. Wu, J. L. Luo, N. L. Wang, L. Viciu, R. J. Cava, and M. Z. Hasan, Phys. Rev. Lett. **96**, 216405 (2006).
[29] T. Berlijn, D. Volja, and W. Ku, Phys. Rev. Lett. **106**, 077005 (2011).
[30] G. A. Burdick, Phys. Rev. **129**, 138 (1963).
[31] G. T. Wang, X. Dai, and Z. Fang, Phys. Rev. Lett. **101**, 066403 (2008).
[32] A. Bourgeois, A. A. Aligia, and M. J. Rozenberg, Phys. Rev. Lett. **102**, 066402 (2009).
[33] D. J. Singh and D. Kasinathan, Phys. Rev. Lett. **97**, 016404 (2006).
[34] B.-B. Zhang, N. Zhang, S.-T. Dong, Y. Lv, Y. B. Chen, S. Yao, S.-T. Zhang, Z.-B. Gu, J. Zhou, I. Guedes, D. Yu, and Y.-F. Chen, AIP Adv. **5**, 087111 (2015).
[35] T. Arakane, T. Sato, T. Takahashi, T. Fujii, and A. Asamitsu, New J. Phys. **13**, 043021 (2011).

[36] N. Kaurav, K. K. Wu, Y. K. Kuo, G. J. Shu, and F. C. Chou, Phys. Rev. B **79**, 075105 (2009).

[37] H. J. Xiang and D. J. Singh, Phys. Rev. B **76**, 195111 (2007).

[38] M. Jonson and G. D. Mahan, Phys. Rev. B **42**, 9350 (1990).

[39] A. Nicolaou, V. Brouet, M. Zacchigna, I. Vobornik, A. Tejeda, A. Taleb-Ibrahimi, P. Le Fèvre, F. Bertran, S. Hébert, H. Muguerra, and D. Grebille, Phys. Rev. Lett. **104**, 056403 (2010).

[40] H. W. Ou, J. F. Zhao, Y. Zhang, B. P. Xie, D. W. Shen, Y. Zhu, Z. Q. Yang, J. G. Che, X. G. Luo, X. H. Chen, M. Arita, K. Shimada, H. Namatame, M. Taniguchi, C. M. Cheng, K. D. Tsuei, and D. L. Feng, Phys. Rev. Lett. **102**, 026806 (2009).

[41] See Supplemental Material at http://link.aps.org/supplemental/10.1103/PhysRevB.96.081109 for additional ARPES data on $K_xRhO_2$.